Research
A SCIENCE PARTNER JOURNAL

RESEARCH ARTICLE

Standardized Volume Power Density Boost in Frequency-Up Converted Contact-Separation Mode Triboelectric Nanogenerators

Zhongjie Li[1,2], Chao Yang[1], Qin Zhang[1], Geng Chen[3], Jingyuan Xu[4], Yan Peng[2,5*], and Hengyu Guo[6*]

[1]School of Mechatronic Engineering and Automation, Shanghai University, Shanghai 200444, P.R. China. [2]Institute of Artificial Intelligence, Shanghai University, Shanghai 200444, P.R. China. [3]National Engineering Research Center of Turbo-Generator Vibration, School of Energy and Environment, Southeast University, Nanjing 210096, P.R. China. [4]Institute of Microstructure Technology, Karlsruhe Institute of Technology, Karlsruhe 76344, Germany. [5]Shanghai Artificial Intelligence Laboratory, Shanghai 200444, P.R. China. [6]Department of Applied Physics, Chongqing University, Chongqing 400044, P.R. China.

*Address correspondence to: pengyan@shu.edu.cn (Y.P.); physghy@cqu.edu.cn (H.G.)

Citation: Li Z, Yang C, Zhang Q, Chen G, Xu J, Peng Y, Guo H. Standardized Volume Power Density Boost in Frequency-Up Converted Contact-Separation Mode Triboelectric Nanogenerators. *Research* 2023;6:Article 0237. https://doi.org/10.34133/research.0237

Submitted 24 July 2023
Accepted 5 September 2023
Published 22 September 2023

Copyright © 2023 Zhongjie Li et al. Exclusive licensee Science and Technology Review Publishing House. No claim to original U.S. Government Works. Distributed under a Creative Commons Attribution License 4.0 (CC BY 4.0).

The influence of a mechanical structure's volume increment on the volume power density (VPD) of triboelectric nanogenerators (TENGs) is often neglected when considering surface charge density and surface power density. This paper aims to address this gap by introducing a standardized VPD metric for a more comprehensive evaluation of TENG performance. The study specifically focuses on 2 frequency-up mechanisms, namely, the integration of planetary gears (PG-TENG) and the implementation of a double-cantilever structure (DC-TENG), to investigate their impact on VPD. The study reveals that the PG-TENG achieves the highest volume average power density, measuring at 0.92 W/m^3. This value surpasses the DC-TENG by 1.26 times and the counterpart TENG by a magnitude of 69.9 times. Additionally, the PG-TENG demonstrates superior average power output. These findings introduce a new approach for enhancing TENGs by incorporating frequency-up mechanisms, and highlight the importance of VPD as a key performance metric for evaluating TENGs.

Introduction

The advent of sensor networks and the proliferation of big data have propelled the Internet of Things (IoT) into a promising technology with vast potential for the future. With the extensive deployment of sensors and a multitude of electronic devices within IoT systems, ensuring dependable power supplies for their daily operations becomes imperative. In large-scale, high-quantity, and widely distributed IoT scenarios, the conventional energy supply, such as electrochemical batteries, proves to be problematic due to the need for regular replacement or recharging, leading to substantial costs. Consequently, researchers and innovators have turned their attention to energy harvesters derived from renewable energy sources as a viable alternative solution over the past few decades. These harvesters work based on several physical effects, including the piezoelectric effect [1–5], the electromagnetic effect [6–9], the triboelectric effect [10,11], and hybrid ones [12–14]. Among them, triboelectric nanogenerators (TENGs) [15,16] have been receiving increasing prevalence due to low cost and high maximum energy conversion efficiency [17].

Since the concept of the TENGs was proposed by Prof. Zhong Lin Wang in 2012 [18], numerous TENGs have been proposed and applied in various fields [19–22], such as signal monitoring [23–25], energy harvesting [26–28], information collection [29–31], and power supply [32–34]. Later, Prof. Wang and his coworkers developed an electro-mechanic model of TENGs [35–37] based on the expansion of Maxwell equations [38–40]. The most common TENGs operate in contact-separation mode. Namely, when 2 different polarized material interfaces come in contact, a charge transfer process occurs, generating a current when an external circuit is connected.

Among the 4 well-known modes of TENGs, contact-separation mode (CS-TENG) has been commonly utilized in low-frequency energy harvesting (10 Hz) [21,41]. For example, Zi et al. [42] revealed that TENGs exhibited a much better output performance, particularly in voltage output, compared with electromagnetic generators under low-frequency motion (typically 0.1 to 3 Hz). Wu et al. [43] presented a mechanical amplifier-assisted TENG with 2 springs, the power density of which was nearly 0.1 to 0.9 mW/m^2 under an excitation of 2.5 Hz to 4.5 Hz. A spherical TENG for water wave energy harvesting exhibited a maximum output power of 16.6 mW [44]. Cheedarala et al. [45] proposed a novel TENG, which produced 75 V and 1 μA of open-circuit voltage and short-circuit current when excited at 6 Hz.

An evident shortcoming of low-frequency CS-TENGs is the high proportion of trivial voltage in one working cycle. Despite high voltage outputs, average power can be drastically low due

to low duty cycle. Therefore, frequency-up mechanisms [46] have been proposed to handle the duty cycle issue. By converting a single low-frequency contact-separation motion to high-frequency oscillations [47], the generated electricity becomes hypothetically much more intensive and responds for a longer time within one excitation cycle [48], leading to a much larger duty ratio and a higher average power.

Gear sets have been proposed as a high-efficiency frequency converting mechanism for the above hypothesis. Kim et al. [49] noticed that the voltage and current of a gear-based TENG system were enhanced 3.6 times and 4.4 times by controlling the gear ratio. To improve the contact frequency, a pair of gears with a governor were used in an automatic switching integrated TENG, and energy regulation was achieved for continuous mechanical energy harvesting [50]. A mechanical transmission module consisting of a gear and cylindrical cam mechanism was installed on a TENG to increase the TENG working frequency and stabilize the output performance. The experimental results showed that an energy extraction efficiency reached as high as 37.8% [51]. This type of frequency-up mechanism was also utilized in lateral sliding-mode TENGs [52,53], exhibiting its high viability.

Besides, the cantilever configuration-based TENG has been proposed to achieve the frequency-up mechanism due to its high-frequency oscillations at low-frequency scenarios. This configuration achieves the frequency-up conversion and performance enhancement due to structural resonance and preset collision between positive and negative tribo layers. Yang et al. [54] proposed a triple-cantilever-based TENG to harvest vibration energy, which doubled the contact-separation cycle in one vibration period. Han et al. [55] fabricated 3 cantilevers with different resonant frequencies and equipped the longest one with a TENG, which generated 20 V peak–peak voltage when excited at 15 Hz. An interacting dual resonant cantilever beam structure TENG was proposed, which achieved an output of 6.2 to 9.8 μW as the frequency ranged from 36.3 Hz to 48.3 Hz [56].

While frequency-up mechanisms undoubtedly enhance the output performance of TENGs in various aspects, the integration of frequency-up conversion mechanical components introduces a trade-off in terms of the overall volume of the TENG. Volume power density (VPD), which is defined as power over the whole device volume, has been considered as a crucial factor to comprehensively evaluate the performance of energy harvesters, especially in the field of piezoelectric and electromagnetic transductions. The prevalence of VPD reveals its high practicability and viability. Despite the popular adoption of surface charge density and surface power density as indicators for assessment, VPD is hereby introduced to address the unclarified issue or trade-off controversy with reported power increase versus device volume increment.

In this paper, we originally and systemically investigate the VPD problem of TENGs with commonly employed frequency conversion mechanisms. The main contributions are as follows: first, a planetary gear TENG (PG-TENG) and a double-cantilever TENG (DC-TENG) are proposed for frequency conversion, and a detailed description of the proposed architecture and working mechanism is presented; second, a systematic investigation of the electrical response of the proposed devices is provided, as well as a comparison of their performance with a CS-TENG as a counterpart; finally, there is a vivid result demonstration of the marked improvement in the average VPD provided by the frequency-up mechanisms.

Results and Discussion

Architecture of frequency-converted TENGs

To fully examine how the increment of volume of TENGs is correlated with power increase as well as VPD and introduce VPD as an evaluation criterion for the frequency-up converted TENG, we designed a PG-TENG with an adjustable gear ratio planetary gear as shown in Fig. 1A. The planetary gear and a rotating plate, which consists of 4 bearings and a disk, are axially fixed in a support frame, for converting contact-separation frequency up. The positive and negative layers are affixed to the surface of a top plate and a bottom plate, respectively. The bottom plate remains static under excitation, while the top plate moves up and down driven by the rotating plate and 2 springs, achieving contact and separation between positive and negative layers. Two sliding bearings and 2 sliding shafts provide smooth movement of the top plate. The triboelectric layers consist of a polyimide substrate, a copper electrode, and 2 triboelectric materials with opposite polarities. Based on the analysis of the schematic structure and the equivalent circuit model, it shows that different materials will not affect the trend of the effect of the frequency-up mechanism on the TENG. Therefore, we only select a couple of materials to be studied in this paper. With characteristics of distinct electron affinity differences and widely adopted as triboelectric materials, Nylon and Teflon are employed as positive and negative layer materials, respectively. The PG-TENG is triggered by the linear direction excitation via a gear and rack drive system (Fig. S1).

Also, we designed a DC-TENG for the high frequency at free oscillation, as illustrated in Fig. 1C. The double-cantilever mechanism is composed of an upper cantilever and a lower cantilever with a tipping point mounted with a mass. The positive and negative layers are adhered to the upper and lower cantilever, respectively, and remain in contact at the initial state. The vibration of the lower cantilever induces contact separation of layers, while the upper cantilever provides elastic contact between the 2 cantilevers. It is noteworthy that triboelectric layers of all TENGs are designed to be completely identical to ensure the effectiveness of the following comparisons. In addition, a counterpart TENG, which is of common composition, is illustrated in Fig. 1B. This simple structure is composed of 2 bases, a pair of triboelectric layers, and a sponge.

Working mechanisms and equivalent circuit model

We interpret the working mechanism of the PG-TENG via the principles of contact electrification and electrostatic induction. Triboelectric layers with different contact states and the power generation principle of the PG-TENG are illustrated in Fig. 2A. At the original state (state I), Bearing 1 rolls into the lowest station and forces 2 triboelectric layers into full contact. According to the principle of contact electrification, the positive Nylon film loses its surface charge while the negative material (Teflon) receives the surface charge till the electrostatic equilibrium is achieved. As Bearing 1 moves to a higher position (state II), the 2 triboelectric layers gradually separate, disrupting the electrostatic equilibrium. Due to difference of surface charge, the Nylon film produces a higher electrical potential than that of the Teflon film. When Bearing 1 starts to leave the Teflon layer and Bearing 2 contacts the Teflon layer (state III), the current flows from the positive electrode to the negative electrode. The 2 triboelectric layers reach the maximum separation distance, and the entire

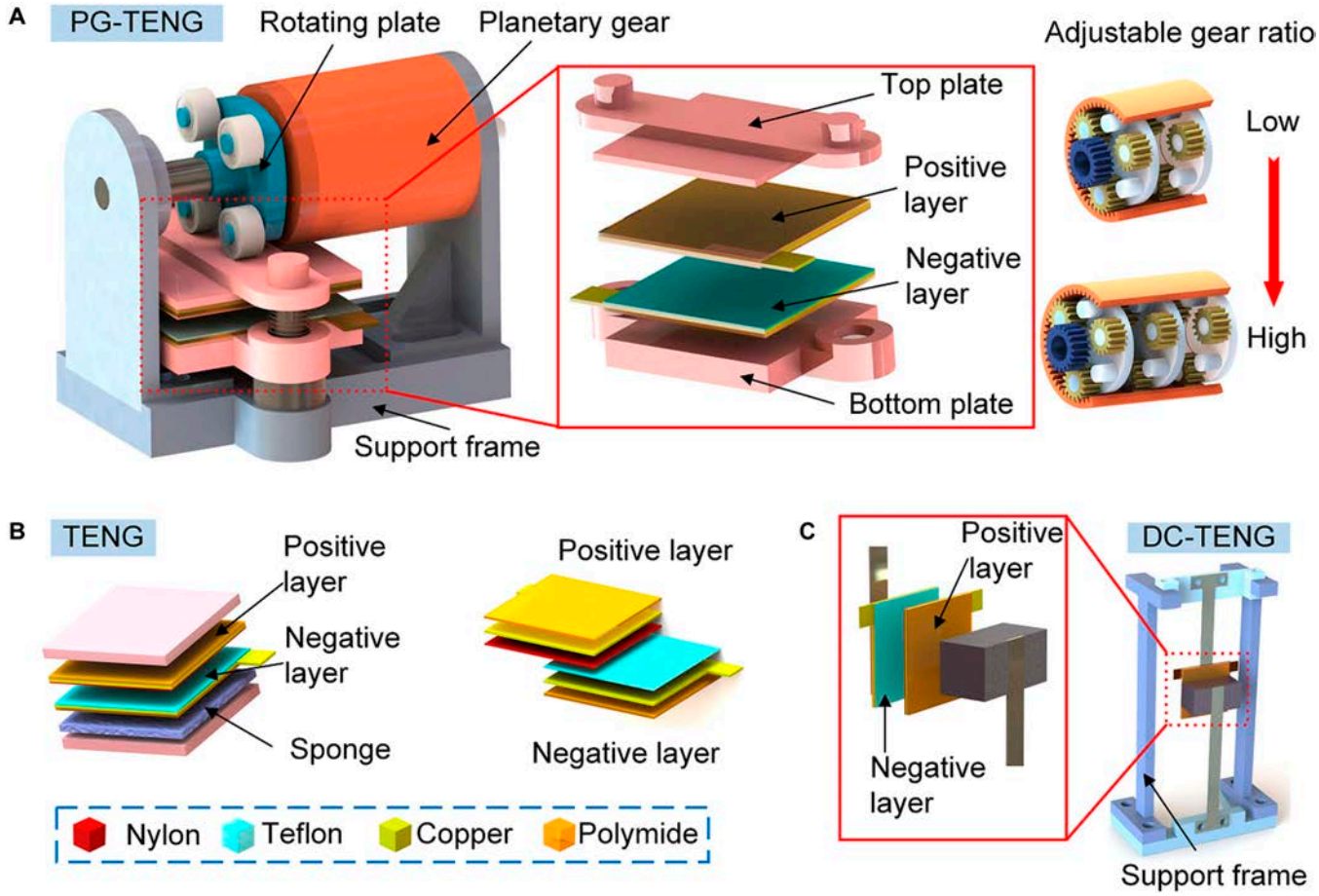


Fig. 1. On frequency-up conversion mechanisms for enhancement in standardized volume power density of triboelectric nanogenerators. (A) Schematic of a planetary gear TENG (PG-TENG). The device is composed of a support frame, a frequency-up part (a planetary gear with adjustable gear ratio and a rotating plate), and a triboelectric part (2 triboelectric layers, 2 plates, 2 sliding bearings, 2 sliding shafts, and 2 springs). (B) Schematic of a contact-separation mode TENG and schematic of triboelectric layers. (C) Schematic of a double-cantilever TENG (DC-TENG). The device is composed of a support frame, 2 cantilevers, a mass, and 2 triboelectric layers.

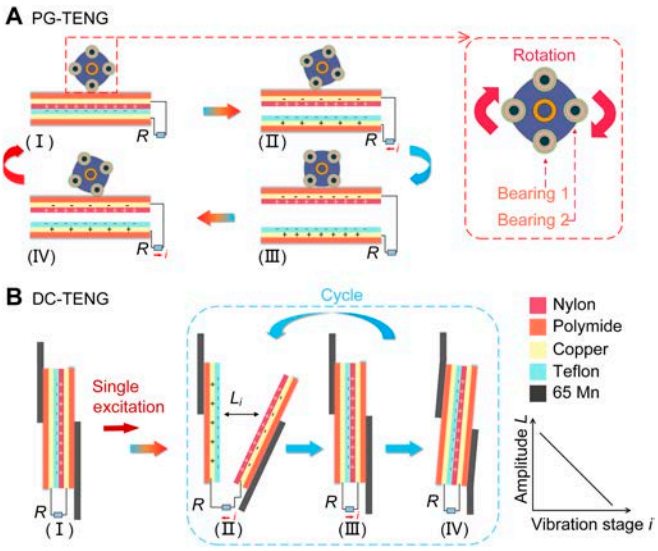


Fig. 2. Working mechanisms of frequency-up mechanism integrated TENGs. Working mechanisms of (A) the PG-TENG and (B) the DC-TENG. Currents are generated by the contact separation of triboelectric layers (CS-TENG). The contact separation of the PG-TENG is provided by the rotation of the rotating plate, while the contact separation of the DC-TENG is provided by the vibration of the lower cantilever with decreasing amplitude (the vibration amplitude decreases with the increment of the vibration stage).

system returns to the electrostatic equilibrium. When Bearing 2 moves to the lowest position (state IV), similar to Bearing 1 in state I, the 2 layers are in progressive contact. Due to the principle of electrostatic induction, the negative charge on the Teflon layer and the positive charge on the Nylon layer generate an induced electrical potential, producing a higher electrical potential on the Teflon layer than the Nylon layer. As a result, the current flows from the negative electrode to the positive electrode.

The planetary gear of the PG-TENG has an input shaft and an output shaft, where the frequency of the output shaft is increased by a definite multiple of the frequency of the input shaft due to the accelerating function of the planetary gear, and this multiple is equal to the gear ratio i of the planetary gear. The frequency of the output shaft f_{out} is given by:

$$f_{out} = if_{in} \tag{1}$$

where f_{in} represents the frequency of the input shaft. The output shaft is connected to the rotating plate that consists of 4 bearings, causing the top plate and the bottom plate to contact-separate 4 times for each rotation of the output shaft. The converted frequency f_p of the PG-TENG can be expressed as:

$$f_p = 4f_{out} = 4if_{in} \tag{2}$$

The input shaft of the PG-TENG is triggered via a gear and rack drive system. According to the characteristics of the motion of the rack and gear, the frequency of the input shaft can be expressed as:

$$f_{in} = \frac{Lf_{exc}}{\pi r} \tag{3}$$

where f_{exc} presents the excitation frequency, L presents the excitation amplitude, and r presents the gear radius of the gear excited by the rack.

Combining Eq. 2 and Eq. 3 gives the converted frequency f_p of the PG-TENG as:

$$f_p = \frac{4f_{exc}iL}{\pi r} \tag{4}$$

The converted frequency f_p is positively proportional to the excitation frequency f_{exc}, the gear ratio i, and the excitation amplitude L.

The expectant frequencies of the PG-TENG are listed in Tables S1 and S2. The difference between the theoretical frequency and the practical frequency is led by the experimental error introduced by the excitation. The practical frequency remains higher than the theoretical frequency. We set the excitation to a uniform linear motion in our theoretical calculations, while the motion of the linear motor can be divided into 3 stages: acceleration, uniform speed, and deceleration. Therefore, the actual speed of the motor during the linear motion phase is faster than the speed used in the theoretical calculation, which results in the practical frequency being higher than the theoretical frequency.

For the transfer process of surface charge and the current generation, the DC-TENG and the CS-TENG exhibit similarities with those of the PG-TENG. The working mechanism of the DC-TENG is illustrated in Fig. 2B. In the initial state (state I), the 2 cantilevers are in contact, and the entire system is at electrostatic equilibrium. Upon linear excitation of the lower cantilever (state II), the current flows from the positive electrode to the negative electrode, and then the lower cantilever bends to its maximum deformation point and the entire system returns to electrostatic equilibrium. Subsequently, as the lower cantilever is released and returns to the initial state (state III), the current flows from the negative electrode to the positive electrode. Then, the lower and the upper cantilevers continue to bend (state IV) until the kinetic energy completely is converted to elastic potential energy. Notably, the DC-TENG can cycle from state II to state IV independently without continuous excitation, owing to the lower cantilever vibration. The inherent frequency (18.37 Hz, simulation by SOLIDWORKS 2018, Fig. S2) is nearly equivalent to the frequency of the current generated by the DC-TENG.

Drawing on Zhao's theory [57], we developed a schematic structure and an equivalent circuit model of the TENG (Fig. 3). We set 1 node in the electrode and 2 nodes in the triboelectric materials. A constant capacitance can be constructed between the adjacent nodes of the electrode and the triboelectric material. A resistance can be set between the nodes in the triboelectric material. Between the neighboring nodes of triboelectric materials, a variable capacitance can be built. Compared to Zhao's theory, applying 2 triboelectric materials rather than one, we expanded the number of nodes from 4 to 6, as shown in Fig. 3. Two constant capacitances C_1 and C_3 are built between Node #1 and Node #2′, and between Node #3′ and Node #4, respectively. A variable capacitance C_2 is constructed between Node #2 and Node #3, and the C_2 varies with the motion of triboelectric layers. R_1 and R_2 are the internal resistances of triboelectric layers. C_0 represents the internal capacitance of TENG, I_0 denotes the internal current of the TENG and Z_L is the load resistance.

According to the model of the contact-separation mode TENG, the open-circuit voltage V_{OC} is:

$$V_{OC} = \frac{\sigma x(t)}{\varepsilon_0} \tag{5}$$

where σ is the surface charge density, $x(t)$ is the separation distance of the 2 triboelectric layers, and ε_0 is the dielectric constant in a vacuum. Equation 5 indicates that the open-circuit voltage V_{OC} is completely independent of frequency. The equivalent resistance R_0 is expressed as:

$$R_0 = \frac{R_1 R_2}{R_1 + R_2} \tag{6}$$

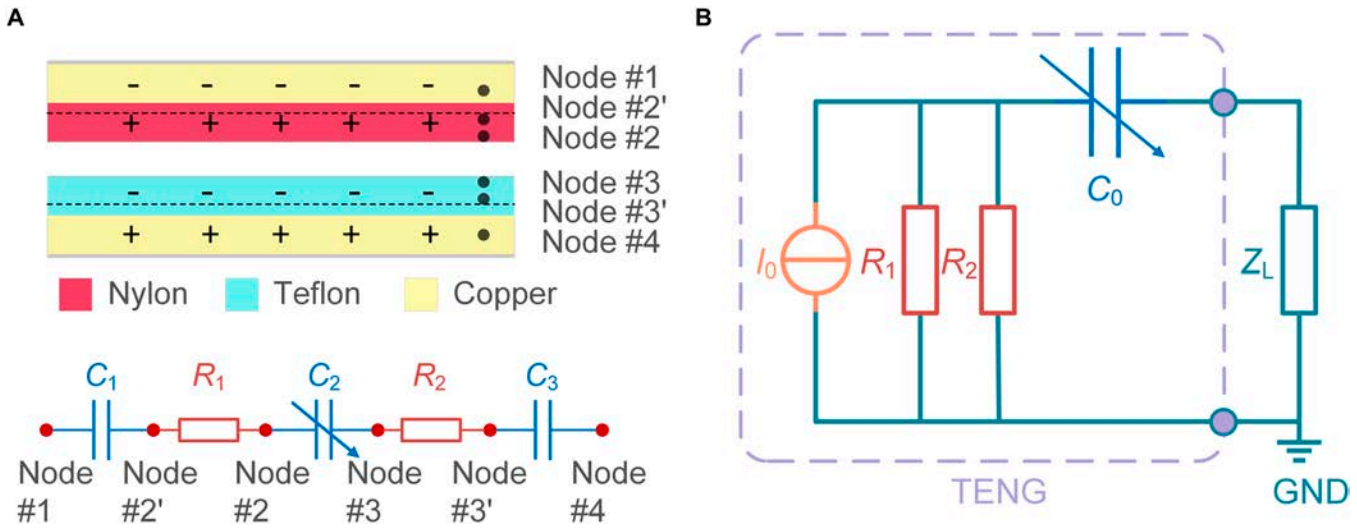


Fig. 3. Schematic structure and equivalent circuit model of the TENG. (A) Schematic structure of the TENG. (B) Equivalent circuit model of the TENG. The TENG consists of 2 electrodes and 2 triboelectric materials with opposite polarity. The TENG is separated by 6 nodes and equated into 5 parts.

where R_1 and R_2 are the internal resistances of triboelectric layers. The equivalent capacitance C_0 is expressed as:

$$C_0 = \frac{1}{C_1} + \frac{1}{C_2} + \frac{1}{C_3} \quad (7)$$

Open-circuit voltage, short-circuit current, and impedance matching

We initially conducted experiments of open-circuit voltages and transferred charge of the TENG under excitations amplitude of 20 mm and speeds ranging from 0.02 m/s to 0.2 m/s (Fig. 4). The open-circuit voltages are approximately 41.87 V, while the transferred charges are approximately 16.37 nC. Notably, the speed or frequency of the TENG solely affects the rate of charges transfer in the closed circuit and imposes no evident influence on the open-circuit voltage and the transferred charges, which agrees well with the indication of the model in Eq. 5.

The following are the comparative experimental results of the short-circuit current of 3 kinds of TENGs under different excitations. The excitation amplitudes were settled into 10 mm and 20 mm, while 3 excitation frequencies (1 Hz, 1.5 Hz, and 2 Hz) were used for each amplitude. As for the PG-TENG, gear ratios of 23 and 64 were selected.

The frequency-up mechanism demonstratively enhances both the amplitude and the frequency of the short-circuit current. The current responses are shown in Fig. 5 and Fig. S3. The PG-TENG demonstrates a noteworthy increase in short-circuit current. Specifically, at the excitation of 2 Hz/10 mm, the PG-TENG produces a peak current of 5.39 μA, which is 4.22 μA higher than that of the TENG. Although the amplitude of the PG-TENG current is consistent under ideal situations, the sustained resistance provided by the PG-TENG will lead to unsmooth excitation. The current curvature exhibits apparent fluctuations (Fig. 5F) due to the unsmooth excitation of the linear motor. The excitation speed is demonstrated in the form of the current in Fig. 5F, and the current response of the PG-TENG is similar to that of the PG-TENG (64). Also, the current gradually increases and decreases with linear motor activation and reduction at the beginning and end of one response cycle. During the middle response stage, the current remains stable due to the constant linear motor speed.

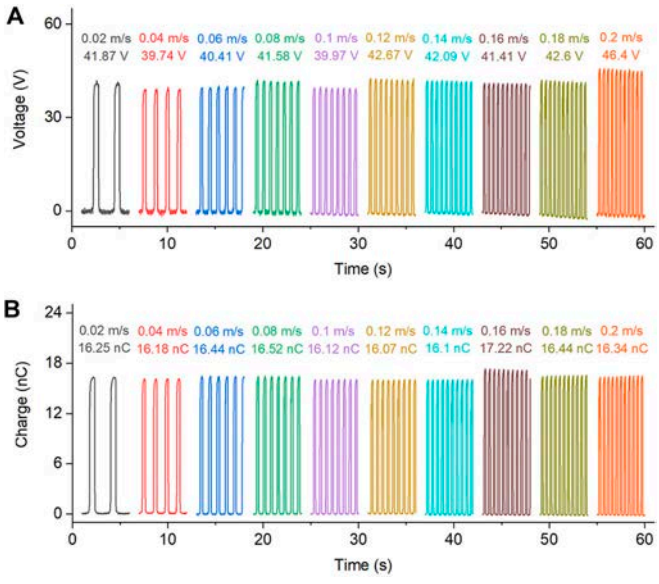


Fig. 4. Open-circuit voltages and transferred charges of the TENG under excitation with 20-mm amplitude and speed from 0.02 m/s to 0.2 m/s. (A) Open-circuit voltages of the TENG, which remain stable and nearly 41.87 V. (B) Transferred charges of the TENG, which remain stable and nearly 16.37 nC.

As for the PG-TENG, the current peak of the PG-TENG with a high gear ratio remains higher than that with a low gear ratio (Fig. 5A to C and Fig. S3). Such results are attributed to the fact that a higher gear ratio leads to a higher-frequency amplification under the same excitation, boosts the speed of transferred charges, and brings about a larger current.

The peak current from the DC-TENG is comparatively much higher than that of the counterpart. Under the excitation of 2 Hz (amplitude being 10 mm), the peak current of the DC-TENG is 4.91 μA, while that of the CS-TENG is 1.17 μA. The highest peak current of the DC-TENG in one excitation period occurs in its first contact-separation period, where maximum impact force is applied and impact speed is provided. The frequency of the DC-TENG current is almost 22 Hz and remains stable as the lower cantilever motion is close to free vibration, and the current frequency is nearly equal to the lower cantilever resonant frequency.

The DC-TENG current amplitude gets gradually attenuated in one excitation period (Fig. 5E). This phenomenon is caused by the rapid decline in the amplitude of the lower cantilever vibration due to intrinsic damping, which, in turn, leads to a declining impact force and contact-separation speed. Remarkably, in contrast with that of the counterpart, the downward trend of the current is linear rather than exponential (Fig. 5E) because of the influence of the upper cantilever and the electrostatic force of triboelectric layers. The upper cantilever provides deceleration in contact motion and acceleration in separation motion, while the electrostatic force provides acceleration in contact motion and deceleration in separation motion.

During the beginning contact-separation periods, the current of the DC-TENG exhibits differences from the typical contact-separation TENG: instead of the usual 2, 4 current peaks are found (Fig. 5E). The first current peak is produced when the lower cantilever comes into contact with the upper cantilever. Then, the lower cantilever continuously bends the upper cantilever and leaves a tiny gap between both triboelectric layers. This tiny gap is filled when the 2 cantilevers go back to their initial states. The creation and disappearance of the tiny gap provide a little separation-contact motion, producing the 2 current peaks in the middle. The last current peak presents when the lower cantilever separates from the upper cantilever.

All examined TENGs exhibit an increase in short-circuit current with a higher excitation frequency. Namely, as shown in Fig. 5A and Fig. 5B, all 3 TENGs generate higher peak currents under the excitation with higher frequency. When excitation (10 mm) frequency goes from 1 Hz to 2 Hz, the peak current of the PG-TENG, DC-TENG, and CS-TENG rises from 4.37 μA, 4.23 μA, and 0.62 μA to 5.39 μA, 4.91 μA, and 1.17 μA, respectively. For the PG-TENG and the CS-TENG, a higher excitation frequency introduces a higher contact-separation motion frequency, leading to an increment in the current. For the DC-TENG, a higher excitation frequency provides higher initial kinetic energy and then increases the contact-separation motion speed and impact force, bringing about a larger current amplitude.

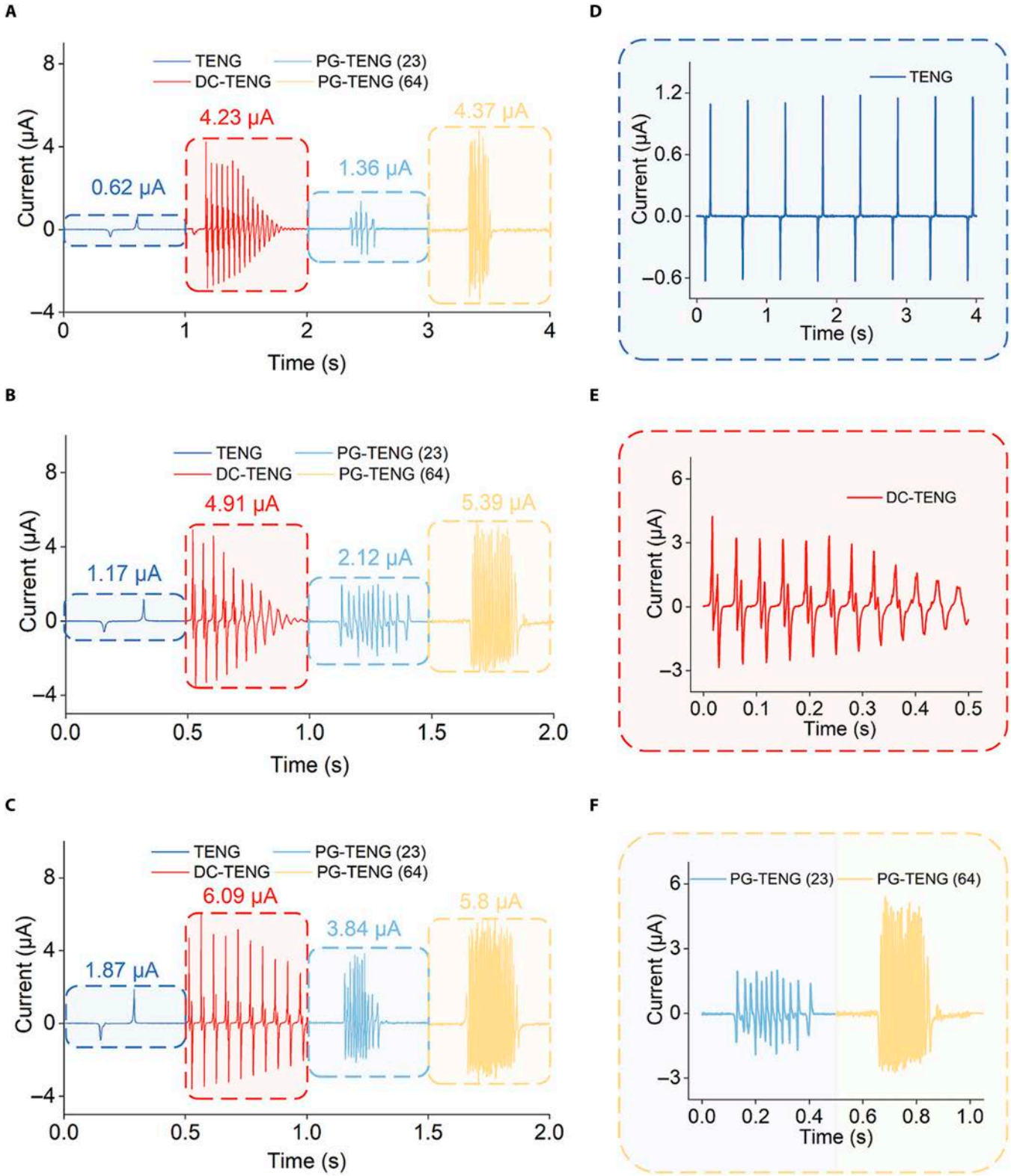


Fig. 5. Comparison of short-circuit current of 4 TENGs. The short-circuit current of 4 TENGs under excitation of (A) 1 Hz/10 mm, (B) 2 Hz/10 mm, and (C) 2 Hz/20 mm. The short-circuit current of (D) the TENG, (E) the DC-TENG, and (F) the PG-TENG (23, 64) under excitation of 2 Hz/10 mm. The PG-TENG exhibited the best frequency conversion effect.

Moreover, the currents of 3 TENGs are positively correlated with the excitation amplitude. The currents of DC-TENG are 4.91 μA and 6.09 μA under excitations of 2 Hz/10 mm and 2 Hz/20 mm. The increase of the excitation amplitude amplifies the initial bending amplitude of the lower cantilever, thus gathering more initial kinetic energy, which results in higher contact-separation motion speed and larger impact force, generating a larger contact force and leading to the current boost of the DC-TENG. Under

the same frequency, a higher-amplitude excitation equals a higher speed excitation, which enhances the contact-separation speed of layers of the PG-TENG and then improves the current. When the excitation frequency is 2 Hz, the currents of the PG-TENG are 5.39 μA and 5.8 μA while the excitation amplitudes are 10 mm and 20 mm. For the CS-TENG, under higher-amplitude excitations and the same frequency, the accelerated contact-separation speed causes an increase in currents, which are 1.17 μA and 1.87 μA under excitations of 2 Hz/10 mm and 2 Hz/20 mm.

The short-circuit current I_{SC} of the contact-separation mode TENG is the variation rate of the transferred charges [58] and is reported as:

$$I_{SC} = \frac{\Delta Q}{\Delta t} \tag{8}$$

where Q is the transferred charges and the t is the time of the charges transfer process. I_{SC} is influenced by the contact-separation speed. The frequency-up mechanism decreases the charge transfer time and then increases the I_{SC}.

To compare the output power of 4 TENGs, the matched impedance of all TENGs was measured (Fig. 6 and Figs. S4 to S7). The frequency-up mechanism effectively reduces the matched impedance. Under the excitation of 2 Hz/20 mm, the matched impedances of the CS-TENG, the DC-TENG, and the PG-TENG are around 11 MΩ, 4 MΩ, and 5 MΩ, respectively. The matched impedances of the PG-TENG and the CS-TENG decrease slowly with the growth of the excitation frequency and excitation amplitude. A higher gear ratio leads to a higher frequency, causing the lowered matched impedance of the PG-TENG. The matched impedance of the DC-TENG is decreased with the rise of the excitation amplitude, which is 5 MΩ and 4 MΩ under the excitation of 10 mm and 20 mm, respectively. According to the schematic structure and an equivalent circuit model we built, the internal resistance Z_i is written as:

$$Z_i = \sqrt{\left(\frac{R_1 R_2}{R_1 + R_2}\right)^2 + \left(\frac{1}{2\pi f}\left(\frac{1}{C_1} + \frac{1}{C_2} + \frac{1}{C_3}\right)\right)^2} \tag{9}$$

where f is the current frequency. The matched impedance of TENGs is negatively related to frequency in the second term in Eq. 9, so that as the frequency of the imposed contact force goes up, the impedance gets lowered evidently.

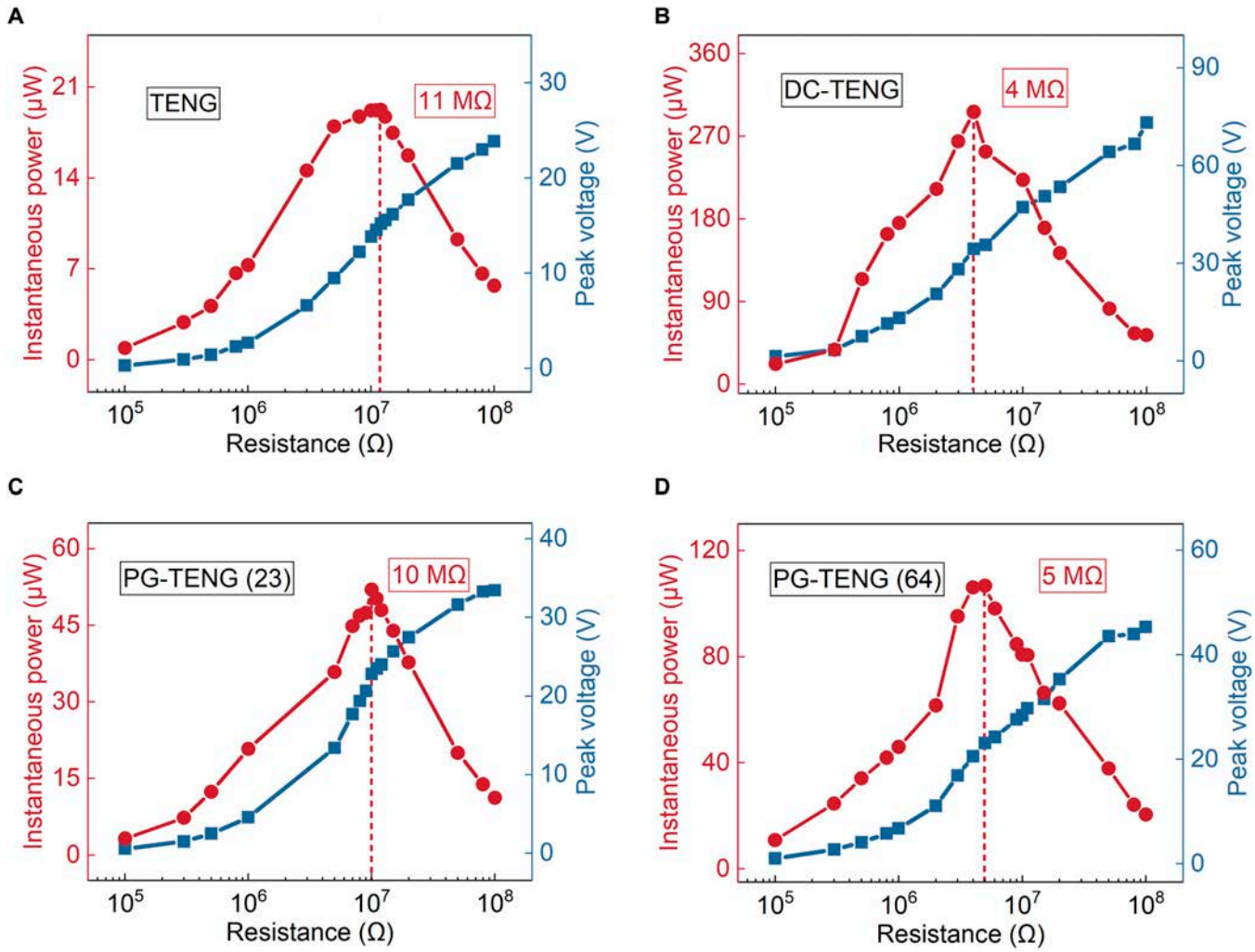


Fig. 6. Matched impedances of TENGs. Matched impedances of (A) the TENG, (B) the DC-TENG, (C) the PG-TENG with a gear ratio of 23, and (D) the PG-TENG with a gear ratio of 64 under excitation with a frequency of 2 Hz and an amplitude of 20 mm. Frequency-up mechanisms decrease the matched impedance.

Power and VPD

Following the investigation of the effect of high frequency on the current and impedance responses, we continued carrying out power experiments and calculated the instantaneous power P_{ins} by:

$$P_{ins} = \frac{{U_L}^2}{R_L} \tag{10}$$

where U_L and R_L are the peak load voltage and the matched resistance, respectively.

The increased load voltage U_L and the decreased matched impedance R_L of frequency-converted TENGs collectively cause the instantaneous power boost. Hence, the PG-TENG and the DC-TENG produce much higher instantaneous power compared with that of the counterpart TENG (Fig. 7A and Fig. S8A), which are 8.86 and 30.66 times higher under the excitation of 2 Hz/10 mm. The increase of excitation frequency and amplitude leads to the instantaneous power growth of the PG-TENG, owing to the increase in the terminal voltage and the lowered matched impedance. Under the excitation amplitude of 10 mm (Fig. 7A), as the excitation frequency rises from 1 Hz to 2 Hz, the instantaneous power of the PG-TENG increases from 26.79 μW to 39.84 μW. When the excitation (2 Hz) amplitude is 20 mm, the PG-TENG generates an instantaneous power of 106.72 μW. The instantaneous power of the PG-TENG is amplified by utilizing a higher gear ratio that provides a better frequency-up conversion effect. Under the excitation of 1 Hz/10 mm, the PG-TENG with a high ratio has 3.86 times the instantaneous power of the PG-TENG with a low ratio.

In the instantaneous power experiments, the DC-TENG shows similarly desirable yields. As shown in Fig. 7D, under the excitation of 1 Hz/10 mm, the instantaneous power of the DC-TENG is 106.72 μW in contrast with 1.33 μW of the CS-TENG. With the rise of the excitation frequency, the load voltage shows a minor improvement, while the increase of the excitation amplitude markedly enhances the load voltage and reduces the matched impedance. Consequently, the instantaneous power of the DC-TENG increases slowly with the increase of the excitation frequency but rapidly rises with the increment of the excitation amplitude. The instantaneous power of the DC-TENG is raised from 106.72 μW to 127.92 μW when the excitation (10 mm) frequency goes from 1 Hz to 2 Hz, while it is 296.53 μW under an excitation of 2 Hz/20 mm.

The instantaneous power of the DC-TENG consistently increases with the frequency and amplitude of the excitation, and the instantaneous power of the TENG also exhibits the same characteristics. The absolute difference in instantaneous power rises as the increment of excitation frequency and excitation amplitude, but measured in terms of amplification, the DC-TENG produces the best amplification at the lowest frequency and amplitude (1 Hz/10 mm).

Based on Zhao's theory [57], the load power P_L equals:

$$P_L = \frac{{I_0}^2 \left(\frac{R_1 R_2}{R_1 + R_2}\right)^2 R_L}{{R_L}^2 + \left(\frac{1}{2\pi f}\left(\frac{1}{C_1} + \frac{1}{C_2} + \frac{1}{C_3}\right)\right)^2} \tag{11}$$

where I_0 represents the internal current. The load power P_L is positively related to the frequency f, which means that a higher frequency offers a larger load power.

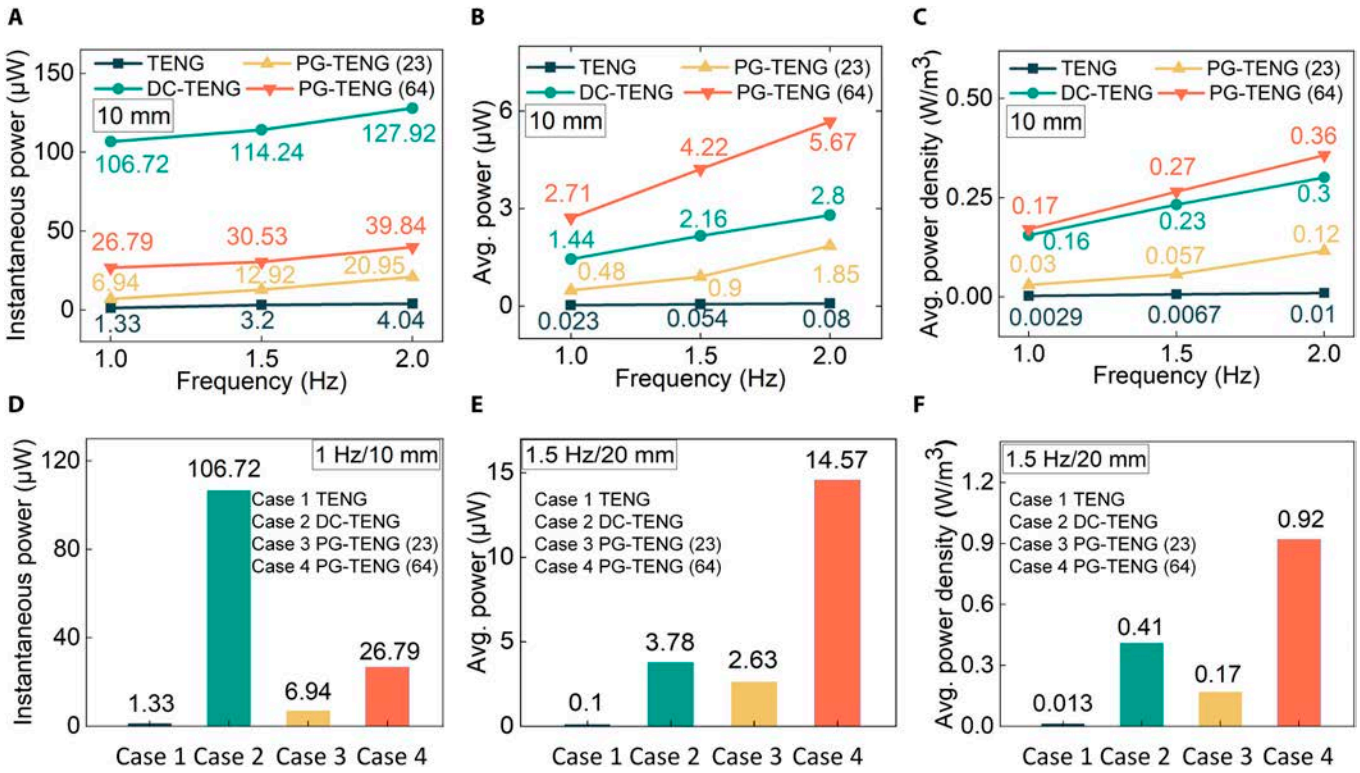


Fig. 7. Power comparison of frequency-up mechanism integrated TENGs and TENG. Comparison of (A) instantaneous power, (B) average power, and (C) average power density of 4 TENGs under 10 mm excitation. (D) Comparison of instantaneous power under 1 Hz/10 mm excitation. (E) Average power and (F) average power density under 1.5 Hz/20 mm excitation. The DC-TENG generates the highest instantaneous power while the PG-TENG reaches the highest average power and average power density.

The average power P_{avg} is calculated as:

$$P_{avg} = \frac{\int_0^T \frac{U_L^2}{R_L} dt}{T} \quad (12)$$

where U_L, R_L, and T are the load voltage, the matched resistance, and the working time, respectively. Experimental results are shown in Fig. 7B and Fig. S8B. Here, considering the short period in one excitation cycle, we employ the actual working cycle T, which corresponds to the time of the current response in Fig. 5F, to calculate the average power of the PG-TENG.

Previous experiments (Fig. 5) have indicated that the frequency-up mechanism can enhance the load voltage U_L and reduce the matched impedance R_L, achieving an average power increment. By converting a single load voltage with low amplitude into multiple load voltages with high and relatively stable amplitude, the PG-TENG exhibits conspicuous improvement and achieves the highest performance in terms of average power. As shown in Fig. 7E, under the excitation of 1.5 Hz/20 mm, the average power of the PG-TENG is 14.57 μW, which is 139.77 times and 2.86 times higher than those of the CS-TENG and the DC-TENG, respectively. The PG-TENG improves the average power distinctly. Even though the average power of the TENG rises with the increase of the excitation frequency and the excitation amplitude, the increase in average power of the PG-TENG is much more rapid. Therefore, the average power of the PG-TENG has a superior amplification than the average power of the TENG under the higher-frequency and larger-amplitude excitation. However, the average power of the PG-TENG is approaching saturation under 1.5 Hz/20 mm excitation, whereas the average power of the TENG is still able to increase under higher-frequency excitation; thus, the optimal condition for the average power of the PG-TENG is 1.5 Hz/20 mm.

Considering that the load voltage is improved and the matched impedance is decreased with the rise of the frequency or amplitude of the excitation, the average power of the PG-TENG is positively correlated with the frequency and amplitude of the excitation. When the excitation (10 mm) frequency goes from 1 Hz to 2 Hz, the average power of the PG-TENG goes from 2.71 μW to 5.67 μW. When excitation (2 Hz) amplitude increases to 20 mm, the average power of the PG-TENG goes up to 17.39 μW. Notably, it is worth pointing out that the average power of the PG-TENG with a high gear ratio is larger than that with a lower ratio.

Although the average power of the DC-TENG is limited by the persistent decrease in its voltage, the double-cantilever frequency-up mechanism still provides notable improvement in average power (Fig. 7B). The average power of the DC-TENG increases with the excitation frequency. The unique structure of the DC-TENG determines that its motion mode is approximately free vibration after a single excitation. During the vibration of the DC-TENG, the power of each contact-separation motion is continuously reduced. The increase in excitation frequency does not markedly increase the speed of the DC-TENG vibration, but it does shorten the time of the DC-TENG vibration so that only the initial contact-separation motions with high power of the DC-TENG are retained, thus increasing the average power. When the excitation (10 mm) frequency goes from 1 Hz to 2 Hz, the average power of the DC-TENG goes from 1.44 μW to 2.8 μW. The increase in excitation amplitude also leads to a rise in the average power of the DC-TENG due to the decrease in the matched impedance and increase in the load voltage. When excitation (2 Hz) amplitude rises to 20 mm, the average power of the DC-TENG increases to 5.13 μW.

As mentioned before, the surface charge density and the surface power density do constrain the parameter of the overall volume of the whole device. This can be of substantial importance particularly when the working space of TENGs are confined. As such, we introduce the volume average power density VPD for evaluating the performance of all TENGs:

$$\mathrm{VPD} = \frac{P_{avg}}{V} \quad (13)$$

where P_{avg} is the average power and V is the necessary dynamic volume. The measured volumes of the TENG, the DC-TENG, and the PG-TENG are 8 cm^3, 9.3 cm^3, and 15.88 cm^3, respectively. Results are presented in Fig. 7C and Fig. S8C.

The experimental results demonstrate that the frequency-conversion mechanisms lead to an evident increase in average VPD compared with that of the CS-TENGs. As shown in Fig. 7F, under the excitation of 1.5 Hz/20 mm, the average VPD of the PG-TENG is 0.92 W/m^3, which is 70.92 and 2.26 times those of the CS-TENG and the DC-TENG. The optimal condition for the average power density is 1.5 Hz/20 mm. The reason for this phenomenon is the same as that of the average power. Besides, the PG-TENG with the high frequency produces a larger volume average power density compared with the case under low frequency. All average VPDs of the frequency-up mechanism integrated TENGs remain consistently higher than that of the CS-TENG (Fig. 7C and Fig. S8C). The volume average power densities of the PG-TENG and the DC-TENG improve with the increase of the excitation frequency and amplitude. This variation trend and the variation reason of the volume average power densities of the PG-TENG and the DC-TENG are consistent with their average power outputs. These results further validate the enhancement of the frequency-up mechanisms in the electric outputs of TENGs especially in short-circuit current, output power, and VPD.

Conclusion

This work comprehensively reports electric responses of high-frequency TENGs and settled the controversy on the feasibility of adding extra mechanical components for frequency-up conversion exemplified by 2 commonly seen mechanisms. Specifically, we introduce a PG-TENG with a rotating plate and planetary gear to convert frequency and provide various gear ratios. By comparing the VPD of the PG-TENG with that of a counterpart TENG and a DC-TENG, we demonstrate marked enhancement in the VPD. Through experimental investigations and equivalent circuit modeling, the effectiveness of the proposed high-frequency method is validated by the PG-TENG with the highest VPD of 0.92 W/m^3. Furthermore, The PG-TENG exhibits an average power that is 69.92 and 1.26 times higher than those of the CS-TENG and the DC-TENG.

With respect to experimental results of interest, the volume increase in both approaches directly raises the force frequency, turning low-frequency excitations into relatively high ones. As such, the matched impedance is lowered and short-circuit current is enhanced simultaneously. Despite increment in volume, the much enhanced power outputs underline the prominence of this trade-off, especially from the angle of VPD. Future work can be focused on modeling of relation between resultant lowered impedance and short-circuit current under

high-frequency excitations. This study can serve as guidelines for high-performance TENG designs.

Materials and Methods

Fabrication of the triboelectric layers

The built TENGs have identical triboelectric layers with a flat size of 20 mm × 20 mm. We chose a 0.125-mm-thick polyimide film as the substrate, and a copper film with a thickness of 0.05 mm as the electrode, which is directly attached to the substrate. Meanwhile, the positive and negative triboelectric materials are attached to the electrodes. We selected a Nylon film with a thickness of 0.05 mm as positive material, while the negative material was a 0.05-mm-thick Teflon film.

Fabrication of the planetary gear TENG

As shown in Fig. S1, the supports of the PG-TENG are machined and prepared from Al and have an overall dimension of approximately 60 mm × 60 mm × 110 mm. The top plate and the bottom plate are machined and prepared from acrylic. Sliding bearings have an inner diameter of 3 mm, an outer diameter of 7 mm, and a length of 10 mm. Sliding shafts have an outer diameter of 3 mm and a length of 10 mm. The prototype of the PG-TENG is excited via a gear whose module is 0.5 and gear teeth are 40 and a rack with the same module and length of 90 mm.

Fabrication of the DC-TENG

The supports of the PG-TENG are machined and prepared from Al and have an overall dimension of approximately 110 mm × 40 mm × 150 mm, the thickness and length of both cantilevers (65 Mn) are 0.5 mm and 65 mm, while the weight of the mass (steel) is 15.5 g. The DC-TENG is pulled by a claw that is built from machined Al and fixed on the linear motor.

Fabrication of the TENG

The 2 bases of the TENG are made by 3-dimensional printing, the material chosen is Ledo, and their dimensions are 20 mm × 20 mm × 10 mm. The selected sponge size is 20 mm × 20 mm × 10 mm and is glued between the negative triboelectric layer and the negative base. Two bases are attached directly to the ends of the motor and are thus driven by the motor.

Measurement and characterization

As shown in Fig. S1, all prototypes and experimental platforms are placed on a vibration-isolation optical platform. We utilized a force sensor (HZC-T-10 kg), a linear motor, and a motor controller (J-best-P3) to provide linear excitation. The motor controller controls the excitation frequency and amplitude. Besides, voltages and currents were measured by an electrometer (Keithley 6514).

Acknowledgments

Funding: This work was funded by the National Natural Science Foundation of China (Nos. 62001281 and 62225308) and the Shanghai Science and Technology Committee (22dz1204300).
Author contributions: Z.L., Y.P., G.C., and J.X. conceptualized the study. Z.L. and C.Y. constructed experimental prototypes. C.Y. and Q.Z. performed the experiments. C.Y. and H.G. wrote the first draft of the paper. Z.L., Y.P., G.C., and J.X. supervised the study. All authors contributed to and approved the final version of the manuscript. **Competing interests:** The authors declare that they have no competing interests.

Data Availability

The data supporting this study are available from the corresponding author.

Supplementary Materials

Fig. S1. Prototyping and experiment platforms.
Fig. S2. Simulation of inherent frequency of DC-TENG lower cantilever.
Fig. S3. Comparison of short-circuit current of TENGs.
Fig. S4. Matched impedance of TENG.
Fig. S5. Matched impedance of DC-TENG.
Fig. S6. Matched impedance of PG-TENG with a gear ratio of 23.
Fig. S7. Matched impedance of PG-TENG with a gear ratio of 64.
Fig. S8. Power comparison of TENGs.
Table S1. Theoretical and practical frequency of PG-TENG with a gear ratio of 23.
Table S2. Theoretical and practical frequency of PG-TENG with a gear ratio of 64.

References

1. Wang M, Yin P, Li Z, Sun Y, Ding J, Luo J, Xie S, Peng Y, Pu H. Harnessing energy from spring suspension systems with a compressive-mode high-power-density piezoelectric transducer. *Energy Convers Manag*. 2020;220(220C):113050.
2. Li Z, Peng X, Hu G, Zhang D, Xu Z, Peng Y, Xie S. Towards real-time self-powered sensing with ample redundant charges by a piezostack-based frequency-converted generator from human motions. *Energy Convers Manag*. 2022;258:115466.
3. Peng Y, Xu Z, Wang M, Li Z, Peng J, Luo J, Xie S, Pu H, Yang Z. Investigation of frequency-up conversion effect on the performance improvement of stack-based piezoelectric generators. *Renew Energy*. 2021;172:551–563.
4. Wang B, Long Z, Hong Y, Pan Q, Lin W, Yang Z. Woodpecker-mimic two-layer band energy harvester with a piezoelectric array for powering wrist-worn wearables. *Nano Energy*. 2021;89(9801):Article 106385.
5. Li Z, Zhao L, Wang J, Yang Z, Peng Y, Xie S, Ding J. Piezoelectric energy harvesting from extremely low-frequency vibrations via gravity induced self-excited resonance. *Renew Energy*. 2023;204:546–555.
6. Peng Y, Zhang D, Luo J, Xie SR, Pu HY, Li ZJ. Harnessing kinetic energy from human motions with a high-efficiency wearable electromagnetic energy harvester. Paper presented at: Proceedings of the ASME 2020 conference on smart materials, adaptive structures and intelligent systems (SMASIS 2020); 2020 Sep 15; online.
7. Li Z, Liu Y, Yin P, Peng Y, Luo J, Xie S, Pu H. Constituting abrupt magnetic flux density change for power density improvement in electromagnetic energy harvesting. *Int J Mech Sci*. 2021;198:106363.
8. Cao H, Kong L, Tang M, Zhang Z, Wu X, Lu L, Li D. An electromagnetic energy harvester for applications in a high-speed rail pavement system. *Int J Mech Sci*. 2022;243(1):108018.

9. Li Z, Jiang X, Yin P, Tang L, Wu H, Peng Y, Luo J, Xie S, Pu H, Wang D. Towards self-powered technique in underwater robots via a high-efficiency electromagnetic transducer with circularly abrupt magnetic flux density change. *Appl Energy*. 2021;302(7):117569.
10. Shen F, Li Z, Guo H, Yang Z, Wu H, Wang M, Luo J, Xie S, Peng Y, Pu H. Recent advances towards ocean energy harvesting and self-powered applications based on triboelectric nanogenerators. *Adv Electron Mater*. 2021;7(9):2100277.
11. Qiao H, Zhang Y, Huang Z, Wang Y, Li D, Zhou H. 3D printing individualized triboelectric nanogenerator with macro-pattern. *Nano Energy*. 2018;50:126–132.
12. Li Z, Luo J, Xie S, Xin L, Guo H, Pu H, Yin P, Xu Z, Zhang D, Peng Y, et al. Instantaneous peak 2.1 W-level hybrid energy harvesting from human motions for self-charging battery-powered electronics. *Nano Energy*. 2021;81:105629.
13. Xie W, Gao L, Wu L, Chen X, Wang F, Tong D, Zhang J, Lan J, He X, Mu X, et al. A nonresonant hybridized electromagnetic-triboelectric nanogenerator for irregular and ultralow frequency blue energy harvesting. *Research*. 2021;2021 (41, article 1807241):1–12.
14. Gao X, Li Z, Wu J, Xin X, Shen X, Yuan X, Yang J, Chu Z, Dong S. A piezoelectric and electromagnetic dual mechanism multimodal linear actuator for generating macro- and nanomotion. *Research*. 2019;2019:8232097.
15. Chun JS, Ye BU, Lee JW, Choi D, Kang CY, Kim SW, Wang ZL, Baik JM. Boosted output performance of triboelectric nanogenerator via electric double layer effect. *Nat Commun*. 2016;7:12985.
16. Huo Z-Y, Kim Y-J, Suh I-Y, Lee D-M, Lee JH, Du Y, Wang S, Yoon H-J, Kim S-W. Triboelectrification induced self-powered microbial disinfection using nanowire-enhanced localized electric field. *Nat Commun*. 2021;12(1):3693.
17. Xie Y, Wang S, Niu S, Lin L, Jing Q, Yang J, Wu Z, Wang ZL. Grating-structured freestanding triboelectric-layer nanogenerator for harvesting mechanical energy at 85% total conversion efficiency. *Adv Mater*. 2014;26(38):6599–6607.
18. Fan F-R, Tian Z-Q, Lin Wang Z. Flexible triboelectric generator. *Nano Energy*. 2012;1(2):328–334.
19. He W, Liu W, Fu S, Wu H, Shan C, Wang Z, Xi Y, Wang X, Guo H, Liu H, et al. Ultrahigh performance triboelectric nanogenerator enabled by charge transmission in interfacial lubrication and potential decentralization design. *Research*. 2021;2021:9812865.
20. Xie L, Zhai N, Liu Y, Wen Z, Sun X. Hybrid triboelectric nanogenerators: From energy complementation to integration. *Research*. 2021;2021:9143762.
21. Tao K, Yi H, Yang Y, Chang H, Wu J, Tang L, Yang Z, Wang N, Hu L, Fu Y, et al. Origami-inspired electret-based triboelectric generator for biomechanical and ocean wave energy harvesting. *Nano Energy*. 2020;67:104197.
22. Chen X, Wang F, Zhao Y, Wu P, Gao L, Ouyang C, Yang Y, Mu X. Surface plasmon effect dominated high-performance triboelectric nanogenerator for traditional chinese medicine acupuncture. *Research*. 2022; 2022:9765634.
23. Tian J, Wang F, Ding Y, Lei R, Shi Y, Tao X, Li S, Yang Y, Chen X. Self-powered room-temperature ethanol sensor based on brush-shaped triboelectric nanogenerator. *Research*. 2021;2021:8564780.
24. Ge X, Gao Z, Zhang L, Ji H, Yi J, Jiang P, Li Z, Shen L, Sun X, Wen Z. Flexible microfluidic triboelectric sensor for gesture recognition and information encoding. *Nano Energy*. 2023;113:108541.
25. Chen Y, Gao Z, Zhang F, Wen Z, Sun X. Recent progress in self-powered multifunctional e-skin for advanced applications. *Exp Dermatol*. 2022;2(1):20210112.
26. Kim H, Hwang HJ, Huynh ND, Pham KD, Choi K, Ahn D, Choi D. Magnetic force enhanced sustainability and power of cam-based triboelectric nanogenerator. *Research*. 2021;2021:6426130.
27. Yang W, Gao Q, Xia X, Zhang X, Lu X, Yang S, Cheng T, Wang ZL. Travel switch integrated mechanical regulation triboelectric nanogenerator with linear–rotational motion transformation mechanism. *Extre Mech Lett*. 2020;37:100718.
28. Xie X, Fang Y, Lu C, Tao Y, Yin L, Zhang Y, Wang Z, Wang S, Zhao J, Tu X, et al. Effective interfacial energy band engineering strategy toward high-performance triboelectric nanogenerator. *Chem Eng J*. 2023;452(Pt 4):139469.
29. Zhang Y, Li Y, Cheng R, Shen S, Yi J, Peng X, Ning C, Dong K, Wang ZL. Underwater monitoring networks based on cable-structured triboelectric nanogenerators. *Research*. 2022;2022:9809406.
30. Song L, Zhang Z, Xun X, Xu L, Gao F, Zhao X, Kang Z, Liao Q, Zhang Y. Fully organic self-powered electronic skin with multifunctional and highly robust sensing capability. *Research*. 2021;2021:9801832.
31. Peng P, Zhou J, Liang L, Huang X, Lv H, Liu Z, Chen G. Regulating thermogalvanic effect and mechanical robustness via redox ions for flexible quasi-solid-state thermocells. *Nano-Micro Lett*. 2022;14(1):81.
32. Lu S, Lei W, Wang Q, Liu W, Li K, Yuan P, Yu H. A novel approach for weak current signal processing of self-powered sensor based on TENG. *Nano Energy*. 2022;103:107728.
33. Zeng Y, Cheng Y, Zhu J, Jie Y, Ma P, Lu H, Cao X, Wang ZL. Self-powered sensors driven by Maxwell's displacement current wirelessly provided by TENG. *Appl Mater Today*. 2022;27:101375.
34. Xie L, Yin L, Liu Y, Liu H, Lu B, Zhao C, Khattab TA, Wen Z, Sun X. Interface engineering for efficient raindrop solar cell. *ACS Nano*. 2022;16(4):5292–5302.
35. Tao XL, Nie JH, Li SY, Shi YX, Lin SQ, Chen XY, Wang ZL. Effect of photo-excitation on contact electrification at liquid-solid interface. *ACS Nano*. 2021;15(6):10609–10617.
36. Wang ZL. On the expanded Maxwell's equations for moving charged media system-general theory, mathematical solutions and applications in TENG. *Mater Today*. 2022;52(141):348–363.
37. Wang ZL, Wang AC. On the origin of contact-electrification. *Mater Today*. 2019;30:34–51.
38. Shao JJ, Willatzen M, Wang ZL. Theoretical modeling of triboelectric nanogenerators (TENGs). *J Appl Phys*. 2020;128(11):111101.
39. Wang ZL. On the first principle theory of nanogenerators from Maxwell's equations. *Nano Energy*. 2020;68:104272.
40. Wang ZL. Maxwell's equations for a mechano-driven, shape-deformable, charged-media system, slowly moving at an arbitrary velocity field v(r,t). *J Phys Commun*. 2022;6(8):085013.
41. Zhang C, Zhao Z, Yang O, Yuan W, Zhou L, Yin X, Liu L, Li Y, Wang ZL, Wang J. Bionic-fin-structured triboelectric nanogenerators for undersea energy harvesting. *Adv Mater Technol*. 2020;5(9):2000531.

42. Zi YL, Guo HY, Wen Z, Yeh MH, Hu CG, Wang ZL. Harvesting low-frequency (< 5 Hz) irregular mechanical energy: A possible killer application of triboelectric nanogenerator. *ACS Nano*. 2016;10(4):4797–4805.
43. Wu C, Liu R, Wang J, Zi Y, Lin L, Wang ZL. A spring-based resonance coupling for hugely enhancing the performance of triboelectric nanogenerators for harvesting low-frequency vibration energy. *Nano Energy*. 2017;32:287–293.
44. Liang X, Liu Z, Feng Y, Han J, Li L, An J, Chen P, Jiang T, Wang ZL. Spherical triboelectric nanogenerator based on spring-assisted swing structure for effective water wave energy harvesting. *Nano Energy*. 2021;83(35):105836.
45. Cheedarala RK, Duy LC, Ahn KK. Double characteristic BNO-SPI-TENGs for robust contact electrification by vertical contact separation mode through ion and electron charge transfer. *Nano Energy*. 2018;44:430–437.
46. Zou Y, Xu J, Fang Y, Zhao X, Zhou Y, Chen J. A hand-driven portable triboelectric nanogenerator using whirligig spinning dynamics. *Nano Energy*. 2021;83:105845.
47. Yun Y, Jang S, Cho S, Lee SH, Hwang HJ, Choi D. Exo-shoe triboelectric nanogenerator: Toward high-performance wearable biomechanical energy harvester. *Nano Energy*. 2021;80:105525.
48. Han K-W, Kim J-N, Rajabi-Abhari A, Bui V-T, Kim J-S, Choi D, Oh I-K. Long-lasting and steady triboelectric energy harvesting from low-frequency irregular motions using escapement mechanism. *Adv Energy Mater*. 2021;11(4):2002929.
49. Kim W, Hwang HJ, Bhatia D, Lee Y, Baik JM, Choi D. Kinematic design for high performance triboelectric nanogenerators with enhanced working frequency. *Nano Energy*. 2016;21:19–25.
50. Pham KD, Bhatia D, Huynh ND, Kim H, Baik JM, Lin Z-H, Choi D. Automatically switchable mechanical frequency regulator for continuous mechanical energy harvesting via a triboelectric nanogenerator. *Nano Energy*. 2021;89(4):106350.
51. Wu H, Li H, Wang X. A high-stability triboelectric nanogenerator with mechanical transmission module and efficient power management system. *J Micromech Microeng*. 2020;30(11):115017.
52. Lu X, Xu Y, Qiao G, Gao Q, Zhang X, Cheng T, Wang ZL. Triboelectric nanogenerator for entire stroke energy harvesting with bidirectional gear transmission. *Nano Energy*. 2020;72:104726.
53. Yoo J, Yoo D, Lee S, Sim J-Y, Hwang W, Choi D, Kim DS. Extremely high and elongated power output from a mechanical mediator-assisted triboelectric nanogenerator driven by the biomechanical energy. *Nano Energy*. 2019;56:851–858.
54. Yang W, Chen J, Zhu G, Wen X, Bai P, Su Y, Lin Y, Wang Z. Harvesting vibration energy by a triple-cantilever based triboelectric nanogenerator. *Nano Res*. 2013;6(12):880–886.
55. Han M, Zhang X, Liu W, Sun X, Peng X, Zhang H. Low-frequency wide-band hybrid energy harvester based on piezoelectric and triboelectric mechanism. *Sci Chin-Technol Sci*. 2013;56(8):1835–1841.
56. Zhang Y, Wang T, Zhang A, Peng Z, Luo D, Chen R, Wang F. Electrostatic energy harvesting device with dual resonant structure for wideband random vibration sources at low frequency. *Rev Sci Instrum*. 2016;87(12):125001.
57. Zhao D, Yu X, Wang J, Gao Q, Wang Z, Cheng T, Wang ZL. A standard for normalizing the outputs of triboelectric nanogenerators in various modes. *Energy Environ Sci*. 2022;15(31):3901–3911.
58. Shan C, He W, Wu H, Fu S, Li G, Du Y, Wang J, Mu Q, Guo H, Liu B, et al. Efficiently utilizing shallow and deep trapped charges on polyester fiber cloth surface by double working mode design for high output and durability TENG. *Nano Energy*. 2022;104:107968.